High-energy solid-state asymmetric supercapacitor based on nickel vanadium oxide/NG and iron vanadium oxide/NG electrodes

Meng Guo[a,b], Jayaraman Balamurugan[a], Nam Hoon Kim[a,**], Joong Hee Lee[a,c,*]

[a] Advanced Materials Institute of BIN Convergence Technology (BK21 Plus Global) & Department of BIN Convergence Technology, Chonbuk National University, Jeonju, Jeonbuk, 54896, Republic of Korea
[b] Department of Biological and Chemical Engineering, Nanyang Institute of Technology, Nanyang, 473000, China
[c] Carbon Composite Research Centre, Department of Polymer - Nano Science and Technology, Chonbuk National University, Jeonju, Jeonbuk, 54896, Republic of Korea

ARTICLE INFO

ABSTRACT

Solid-state supercapacitors (SCs) are well-known as one of the most competitive power sources for modern electronics. However, most of the reported solid-state SCs suffer from low specific capacitance and energy density. Herein, a novel strategy for the synthesis of nickel vanadium oxide ($Ni_3V_2O_8$) and iron vanadium oxide (Fe_2VO_4) nanoparticles (NPs) anchored nitrogen doped graphene (NG) for high energy solid-state asymmetric SC (ACS) through a simple and cost-effective hydrothermal technique was demonstrated. SEM and TEM analysis reveals that active $Ni_3V_2O_8$ and Fe_2VO_4 NPs with uniform size are anchored on NG sheets. Electrochemical performance of $Ni_3V_2O_8$/NG and Fe_2VO_4/NG electrodes showed that both have ultra-high specific capacitances ($\sim$1898 F g^{-1} and 590 F g^{-1} at current density of 1 A g^{-1}, respectively), tremendous rate capabilities, and superior cycling stabilities. Most significantly, solid-state ASC consisting of $Ni_3V_2O_8$/NG as a cathode and Fe_2VO_4/NG as an anode which achieves a high energy density of $\sim$77.2 W h kg^{-1} at a power density of 863 W kg^{-1} and an ultra-long cycle life (capacitance retention of $\sim$83.3% after 20,000 cycles). This study emphasizes the development of a wide variety of energy storage systems for modern electronics.

1. Introduction

Recently, the exhaustion of non-renewable resources and increasing concerns for environmental pollution caused by conventional energy technologies stimulates the urgent necessity of sustainable and high-performance energy configurations [1–3]. Among the energy storage devices, supercapacitors (SCs) have attracted tremendous interests in the global research community due to their exceptional electrochemical properties such as fast charge-discharge rate, predominant power density, and ultra-long cycle life [4,5]. However, the poor energy density of SCs limits their large-scale energy storage device application at industrial sector. In this context, constructing asymmetric SC (ASC) is one of the best choices to enhance the energy density of SCs because the ASC configurations could further increase the operating potential window by integrating positive and negative electrodes with well-separated potential windows [6,7]. Specifically, solid-state ASCs have emerged as promising power supplies because they avoid the electrolyte leaking problem that occurs in traditional aqueous electrolyte-based ASCs [8]. To explore a new type of electrode materials with excellent properties such as high electric conductivities, large specific surface area and unique porous architecture are the key issues to realize high energy ASCs without forfeiting power density and cycling stability [9].

Transition metal oxides (TMOs) have been extensively used as electrode materials in SC applications due to their unique electrochemical properties such as high theoretical capacitance and Faradaic redox characteristics [10]. Binary TMOs offer superior electrochemical properties than monometallic oxide because of their enriched redox kinetics involving multiple oxidation states of different elements. Numerous researches have been reported that binary TMOs such as $NiCo_2O_4$ hollow spheres [11], coaxial $CoMoO_4$ nanowire arrays [12], and $ZnCo_2O_4$ nanorods [13] as promising electrode materials for SCs due to the favorable properties such as low-cost and eco-friendliness. Among the binary TMOs, vanadium based binary MOs have been considered as attractive electrode materials for SCs due to their unique properties including high theoretical capacitance and moderate

working potential window. They are especially suitable for the solid-state electrolyte because of the electrode materials are not easy to degrade even when operating at high temperatures [14]. Furthermore, vanadium-based binary MOs have become as excellent safe host materials for SCs due to the excellent chemical and environmental stability in solid electrolyte as well as the multiple oxidation states of vanadium atom [15]. In specific, nickel vanadium oxide ($Ni_3V_2O_8$) and iron vanadium oxide (Fe_2VO_4) received specific attention in electrochemical applications due to their high electrical conductivity, multiple oxidation states for redox kinetics and cost-effectiveness [16–21]. However, $Ni_3V_2O_8$ and Fe_2VO_4 show disadvantages such as low specific surface area and short cycling life, which confines their electrochemical performance of these electrode materials for practical applications [22]. The serious agglomeration of $Ni_3V_2O_8$ and Fe_2VO_4 reduces the electroactive sites during the electrochemical process, resulting in poor electron transport kinetics and low electrochemical performance. To solve the above-mentioned obstacles, numerous approaches have been proposed to construct suitable conductive supports, which may enhance the electron transport kinetics and reduce the agglomeration of active $Ni_3V_2O_8$ and Fe_2VO_4 nanoparticles (NPs), ensuring a high specific capacitance with excellent rate capacity and outstanding cycling stability.

Graphene has been considered as perfect matrices for supporting active sites because of the ultra-high specific surface area, excellent electric conductivity, outstanding mechanical stability and environmental friendliness [23,24]. Especially, nitrogen doped graphene (NG) is expected to be a better support for $Ni_3V_2O_8$ and Fe_2VO_4 NPs due to their more valence electrons in the carbon architecture, hence deliver the high electron transfer kinetics and boost the electrochemical performance [25,26]. Firstly, the large specific surface area of NG could suppress the aggregation of electroactive $Ni_3V_2O_8$ and Fe_2VO_4 NPs to make them uniform anchor in NG support. Additionally, the highly conductive NG provides the fast electron transports to facilitate the SCs performance with outstanding durability. Therefore, we anticipated that NG support may prevent the aggregation of $Ni_3V_2O_8$ and Fe_2VO_4 structure and enhance the electrochemical performance towards practical energy storage devices.

Herein, we have reported the synthesis of a novel $Ni_3V_2O_8$ and Fe_2VO_4 anchored NG for constructing solid-state ASC to attain high energy and power densities. These $Ni_3V_2O_8$/NG and Fe_2VO_4/NG hybrids were synthesized through a simple, scalable and cost-effective single-step hydrothermal technique. To the best of our knowledge, there has no reports pertaining to solid-state ASC by using $Ni_3V_2O_8$/NG and Fe_2VO_4/NG hybrids-based electrode materials. The solid-state $Ni_3V_2O_8$/NG//Fe_2VO_4/NG ASC device exhibits the maximum operating potential window of 1.6 V, ultra-high energy density of ~77.2 W h kg^{-1} at a power density of 863 W kg^{-1}, tremendous power density (~22.186 kW kg^{-1} at 53 W h kg^{-1}) and excellent cycling stability (~83.3% capacitance retention of 20,000 cycles). In addition, practical applicability of the solid-state ASC device was established through glowing red light emitting diodes (LEDs). Thus, a strong belief of the current synthesis protocol can be easily translated for the synthesis of several vanadium based bimetallic hybrids towards solid-state energy storage and conversion systems.

2. Experimental

2.1. Synthesis of $Ni_3V_2O_8$/NG hybrid

Graphene oxide (GO) was synthesized from natural graphite powder according to our previously reported research work [27]. The $Ni_3V_2O_8$/NG hybrid was synthesized by a simple, scalable, and cost-effective hydrothermal technique. In details: 0.5 mmol nickel (II) acetate tetrahydrate ($Ni(OCOCH_3)_2\cdot4H_2O$) and 0.5 mmol ammonium metavanadate (NH_4VO_3) were dissolved in 5 mL deionized (DI) water. The 40 mg of GO was dispersed in 40 mL of DI H_2O and then sonicated for 30 min. The mixed metal precursor was added drop wise into GO suspension

(mass ratio of mixed metal precursor: GO is 5:1). 1.5 mmol of urea (NH_2CONH_2) was added to the above mixture and stirred for another 30 min. The final mixture was transferred into an 80 mL Teflon-lined stainless-steel autoclave. The autoclave was sealed and heated at ~180 °C for 10 h after that the reaction mixture was cooled down to room temperature naturally. The as-synthesized material was washed with DI water and ethanol several times to remove the unreacted metal precursors and then finally dried at ~60 °C in vacuum oven. The as-obtained material denoted as $Ni_3V_2O_8$/NG hybrid. For comparison, the $Ni_3V_2O_8$/NG hybrid with different mass ratios (mixed metal precursor: GO ratios 2.5:1, 5:1, and 7.5:1) were synthesized by using the similar procedure. In addition, NiO/NG and V_2O_5/NG hybrids were also synthesized using the similar procedure without $Ni(OCOCH_3)_2\cdot4H_2O$ and NH_4VO_3, respectively. The pristine $Ni_3V_2O_8$ was synthesized using the similar procedure without GO.

2.2. Synthesis of Fe_2VO_4/NG hybrid

The Fe_2VO_4/NG hybrid with 2: 1 mass ratios of mixed metal precursors: GO was synthesized by using the similar synthesis procedure of $Ni_3V_2O_8$/NG hybrid. 0.1 mmol iron chloride hexahydrate ($FeCl_3\cdot6H_2O$) and 0.1 mmol NH_4VO_3 was dissolved in 5 mL DI water and then the precursors solution was added dropwise to 40 mL of DI water containing 60 mg GO. 0.3 mmol NH_2CONH_2 was added to the above mixture and then stirred for 30 min. The above mixture was transferred to 80 mL Teflon-lined stainless-steel autoclave. The autoclave was sealed, and reaction was carried out at ~180 °C for 8 h, then cooled down to room temperature naturally. The mixture was washed with DI water and ethanol for several time to remove the unreacted metal precursors and then dried at 60 °C in a vacuum oven.

2.3. Material characterizations

The morphology and microstructures of the as-prepared materials were tested by field emission scanning electron microscopy (FE-SEM; SUPRA 40 VP; Carl Zeiss, Germany) installed in the Center for University-wide Research Facilities at Chonbuk National University, transmission electron microscopy (TEM), scanning transmission electron microscope (STEM), and energy dispersive X-ray spectroscopy (EDS) mapping (H-7650; Hitachi Ltd., Japan) in the Jeonju center of KBSI. The Brunauer-Emmett-Teller (BET) surface area were explored by N_2 sorption isotherms study (Micromeritics ASAP 2020 Plus). The crystalline nature and chemical composition of as-prepared materials were characterized by powder X-ray diffraction (XRD) patterns (Max 2500 V/PC; Rigaku Corporation, Tokyo, Japan), Raman spectroscopy (Nanofinder 30; Tokyo Instruments Co., Osaka, Japan), and X-ray photoelectron spectroscopy (XPS; Theta Probe; Thermo Fisher Scientific, UK) in the Busan center of KBSI. The electrochemical performance of the electrodes was examined by cyclic voltammetry (CV), galvanostatic charge–discharge measurements (GCD), and electrochemical impedance spectroscopy (EIS) (CHI 660D, USA).

2.4. Electrochemical measurements

The electrochemical performance of individual electrodes was carried out in a three-electrode configuration including Pt foil as a counter electrode, Ag/AgCl as a reference electrode and as-obtained materials as working electrode in 3 M KOH aqueous electrolyte. The working electrode was fabricated as follows: the active material, carbon black, and poly(vinylideneeuoride) (PVDF) were mixed with a mass ratio of 80:10:10 and dispersed in N-methyl-2-pyrrolidinone. The obtained slurry was coated on cleaned Ni foam (1 cm × 1 cm) and then dried at ~60 °C for 48 h in vacuum oven. The mass loading of active material was about 3 mg.

The specific capacitance (*C*) of electrodes were calculated based on the discharge curves according to the following Eq. (1) [28]:

$$C = \frac{2I \int V \, dt}{mV^2 \big|_{Vi}^{Vf}} \quad (1)$$

where I is the discharge current (A), m is the mass loading of active material (g), $\int V dt$ is the integral current area, and V is the applied potential window with initial and final values of V_i and V_f.

2.5. Fabrication of solid-state ASC device

The solid-state ASC device was fabricated using $Ni_3V_2O_8$/NG as a cathode and Fe_2VO_4/NG as anode, NKK TF40 (40 μm thickness, Nippon Kadisha Corporation) as a separator, solid KOH/PVA as an electrolyte. The KOH/PVA gel electrolyte was prepared by mixing 1 g of KOH, 1.5 g of PVA in 18 mL of DI water, and stirring at ~80 °C until the formation of gel electrolyte. Followed by soaking the $Ni_3V_2O_8$/NG and Fe_2VO_4/NG electrodes in the KOH/PVA gel electrolyte separately. Then, the solid-state ASC device was fabricated by assembling the two electrodes with NKK TF40 separator and solidified the gel electrolyte at ambient condition. However, the mass ratio of $Ni_3V_2O_8$/NG cathode and Fe_2VO_4/NG anode was calculated as ~0.57 according to the charge balance ($q_+ = q_-$) and their individual capacitive performance, which was obtained from the following Eq. (2):

$$\frac{m_+}{m_-} = \frac{C_- \times \Delta V_-}{C_+ \times \Delta V_+} \quad (2)$$

where m is the mass, C is the specific capacitance, and ΔV is the applied potential window of cathode (+) and anode (−), respectively.

The energy density (E) and power density (P) were calculated using the following Eqs. (3) and (4):

$$E = \frac{C_{Cell} \Delta V^2}{2} \quad (3)$$

$$P = \frac{E}{t_{disch\,arge}} \quad (4)$$

where C_{cell} is the specific capacitance of solid-state ASC device, ΔV is the applied voltage range, $t_{discharge}$ is the discharge time during GCD process.

3. Results and discussion

Fig. 1 illustrate the schematic representation for the synthesis of $Ni_3V_2O_8$/NG and Fe_2VO_4/NG hybrids by simple, scalable, and cost-effective in-situ hydrothermal technique and employed as electrodes in solid-state ASC. The as-obtained $Ni_3V_2O_8$/NG and Fe_2VO_4/NG electrodes were examined by different structural analysis followed by electrochemical performance of individual electrodes. Finally, the electrodes assemble to construct solid-state ASC device towards practical applications.

The surface morphology of $Ni_3V_2O_8$/NG hybrid was examined by

FE-SEM analysis, as shown in Fig. S1. FE-SEM images of $Ni_3V_2O_8$/NG (5:1) reveal that the ultra-fine $Ni_3V_2O_8$ NPs are homogeneously anchored on NG matrices. In contrast, the pristine $Ni_3V_2O_8$ NPs (Fig. S2), in which all the NPs aggregated together to form a larger size, which designates that the NG matrices could effectively prevent the $Ni_3V_2O_8$ NPs from the agglomeration and degradation during the long-term charge-discharge process. To obtain the optimal condition of $Ni_3V_2O_8$/NG hybrid, the surface morphology of $Ni_3V_2O_8$/NG hybrid with different mass ratios of mixed metal: GO (2.5:1, 5:1, 7.5:1) are explored, as shown in Fig. S3. It's significantly observed that the $Ni_3V_2O_8$/NG hybrid (2.5:1) shows low density of $Ni_3V_2O_8$ NPs anchored in the NG sheets, while the $Ni_3V_2O_8$/NG hybrid (7.5:1) displays serious aggregation of $Ni_3V_2O_8$ NPs on NG sheets that may reduce the utilization of active $Ni_3V_2O_8$ NPs. In the case of $Ni_3V_2O_8$/NG (5:1), high-density of active $Ni_3V_2O_8$ NPs homogeneously anchored on NG matrices, which could effectively boost the electrochemical performance of the electrode materials [29,30]. The elemental composition of $Ni_3V_2O_8$/NG hybrid was confirmed by the EDAX analysis, as shown in Fig. S1c. The EDAX analysis demonstrates that the existence of Ni, V, O, N and C element in the $Ni_3V_2O_8$/NG hybrid, indicating that the $Ni_3V_2O_8$ NPs are successfully anchored in the NG sheets.

The intrinsic morphology of the $Ni_3V_2O_8$/NG hybrid was further investigated by TEM and high resolution TEM (HR-TEM). Fig. 2a and b shows that the $Ni_3V_2O_8$ NPs with the size of ~15–20 nm are anchored on NG sheets. The SAED pattern (inset of Fig. 2a) demonstrates the crystal nature of $Ni_3V_2O_8$/NG hybrid (inset of Fig. 2a). Additionally, the HR-TEM image of $Ni_3V_2O_8$/NG hybrid (Fig. 2c) clearly depicts that the $Ni_3V_2O_8$ NPs are presented as a petal-like structural configuration. This unique structure plays an important role in enhancing the catalytic activity for SCs due to its large specific surface area and surface corners in this structure [31]. Especially, the porously branched petals can shorten the electron transfer pathway and facilitate the charge transport properties, which could effectively improve the electrochemical performance of $Ni_3V_2O_8$/NG hybrid. Fig. 2d and e shows the lattice fringe with interplanar spacing of ~0.32 nm and ~0.14 nm, which corresponds to the (211) and (080) planes of $Ni_3V_2O_8$ (JCPDS 74-1485), respectively. The lattice fringes of $Ni_3V_2O_8$ are extended across the different petal branches without phase separation, which reveals the perfect mixing of nickel and vanadium precursors. The elemental distribution and composition of $Ni_3V_2O_8$/NG hybrid was further investigated by the STEM-EDS mapping analysis (Fig. 2f). Fig. 2f depicts that the N elements are homogeneously doped in graphene matrices. Furthermore, nickel, vanadium and oxygen elements were distributed and incorporated well in the NG sheets. These results further proved that the current synthesis technique provides an efficient route to prepare the $Ni_3V_2O_8$/NG hybrid without any high-temperature conditions. The STEM-EDS line mapping of $Ni_3V_2O_8$/NG hybrid (Fig. S4) shows that the a single $Ni_3V_2O_8$ NPs anchored into NG sheets, further revealing that no phase segregation existed in the $Ni_3V_2O_8$ NPs in the hybrid nanostructure. This result is well-consistent with HR-TEM
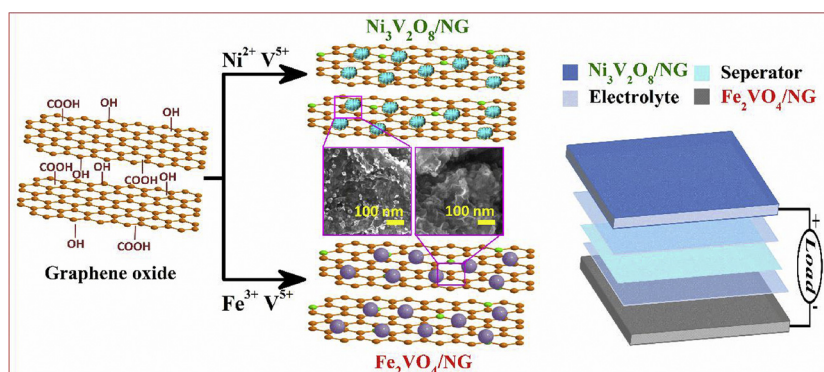

Fig. 1. Schematic illustration of the synthesis of $Ni_3V_2O_8$/NG and Fe_2VO_4/NG hybrids for solid-state ASC.
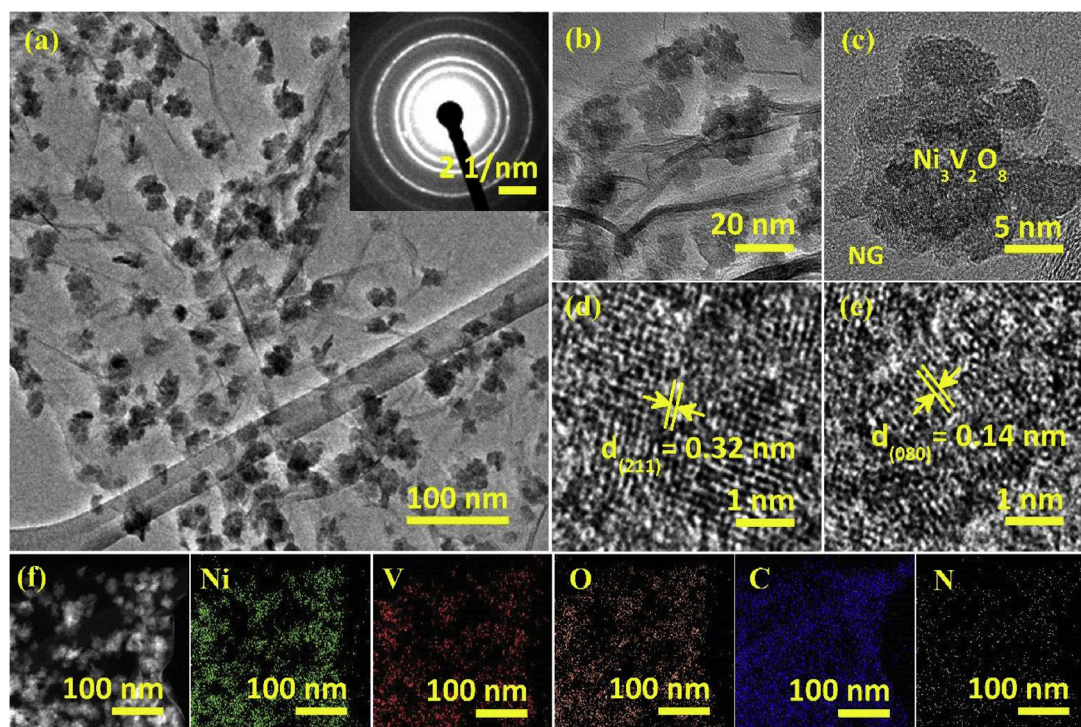
Fig. 2. (a, b) TEM images with different magnifications (inset shows the corresponding SAED pattern), (c–e) HR-TEM images, and (f) STEM-EDS color mapping of $Ni_3V_2O_8$/NG hybrid.

analysis.

Similarly, the morphological analysis was carried out for Fe_2VO_4/NG anode. Fig. S5a and b shows that the Fe_2VO_4 NPs are uniformly anchored in the crumpled NG sheets, which is beneficial to reduce the agglomeration of Fe_2VO_4 NPs and enhance the cycling performance during consecutive charge-discharge process. Fig. S5c displays the EDAX analysis of Fe_2VO_4/NG hybrid, indicating the successful doping of N elements into the graphene sheets. TEM images of Fe_2VO_4/NG hybrid (Fig. 3a) reveal that the Fe_2VO_4 NPs with an average size of $\sim$15–20 nm anchored into the ultra-thin NG sheets, which could be further confirmed by STEM image of Fe_2VO_4/NG hybrid, as shown in Fig. 3b. In addition, The HR-TEM shows that the microporous Fe_2VO_4 NPs were anchored on NG sheets in the Fe_2VO_4/NG hybrid (Fig. 3c). This hierarchical structure of Fe_2VO_4/NG hybrid suggests that the NG sheets can forcefully suppress the growth and aggregation of Fe_2VO_4 NPs, resulting in the large surface area and enhanced electrochemical performance of Fe_2VO_4/NG hybrid. The lattice fringe with interplanar spacing of $\sim$0.15 nm was shown in Fig. 3d, corresponding to the (440) plane of Fe_2VO_4 (JCPDS 75-1519). The FFT pattern of the Fe_2VO_4/NG hybrid (Fig. 3e) indicates the polycrystalline nature. The highly crystalline Fe_2VO_4 texture anchored on NG sheets, which is perceived from the hydrothermal reaction [32]. Fig. 3f depicts the STEM-EDS line mapping clearly reveals that the successful alloy formation and elemental doping of the Fe_2VO_4/NG hybrid. Likewise, there is strong white contract in the Fe_2VO_4 species is due to the atomic number of the FeV alloy is relatively higher than N and C elements in the Fe_2VO_4/NG hybrid. The N and C signals are received from support of the hybrid. The EDAX color mapping further demonstrates the active Fe_2VO_4 NPs are homogeneously anchored on NG sheets in the Fe_2VO_4/NG hybrid (Fig. S6).

It is well known that the active electrode materials with an extraordinary specific surface area can increase the electroactive sites and enhance the electrochemical performance of SCs. Therefore, N_2 sorption isotherm analysis was used to examine the specific surface area of $Ni_3V_2O_8$/NG and Fe_2VO_4/NG hybrids (Fig. 4a and b). The N_2 sorption isotherms of both $Ni_3V_2O_8$/NG and Fe_2VO_4/NG hybrids display the

hysteresis loops between the relative pressure (P/P_0) of $\sim$0.45 to 1.0, which belong to the typical type-IV isotherm, indicating the existence of mesoporous structure in the electrode materials. The Barret–Joyner–Halenda (BJH) pore size distribution (inset of Fig. 4a and b) is calculated from the desorption isotherm, which shows that the pore diameters of $Ni_3V_2O_8$/NG and Fe_2VO_4/NG are around 3.5 nm and 3.6 nm, which is mainly contributed from the internal space of active $Ni_3V_2O_8$ and Fe_2VO_4 NPs, respectively. This result also corresponds to their mesoporous architecture. Due to this porous structure, the $Ni_3V_2O_8$/NG and Fe_2VO_4/NG hybrids exhibit the large BET specific surface areas of $\sim$203 $m^2\,g^{-1}$ and $\sim$252 $m^2\,g^{-1}$, respectively. Such a high specific surface area with a unique mesoporous structure is advantageous to shorten the ion diffusion pathways and boost the electrochemical performances of the $Ni_3V_2O_8$/NG and Fe_2VO_4/NG hybrids [33].

To further exploit the crystal structure, the XRD pattern of $Ni_3V_2O_8$/NG and Fe_2VO_4/NG hybrids are shown in Fig. 4c. A broad diffraction peak at about $\sim$26.1° appeared in both $Ni_3V_2O_8$/NG and Fe_2VO_4/NG hybrids, attributing to the (002) plane of graphite originated from the NG sheets. Such a hump represents the highly disordered NG sheets with a graphitization degree and the active $Ni_3V_2O_8$ and Fe_2VO_4 NPs active sites are strongly anchored into NG sheets [34,35]. However, the $Ni_3V_2O_8$/NG hybrid displays that the diffraction peaks are corresponding to the (131), (122), (331), (242), (213), (162) and (442) crystal plane of $Ni_3V_2O_8$ (JCPDS 74-1485) [36]. In the case of Fe_2VO_4/NG hybrid, the diffraction peaks can be ascribed to the (220), (311), (400), (422), (511) and (440) planes of Fe_2VO_4 (JCPDS 75-1519) [37]. These results are well-consistent with the HR-TEM analysis. Raman spectroscopy is one of the effective technique to investigate the structural property of carbon-based materials. Fig. 4d shows that the Raman spectra of $Ni_3V_2O_8$/NG and Fe_2VO_4/NG hybrids. The D band located at $\sim$1351 cm^{-1} and G band located at $\sim$1593 cm^{-1} are assigned to the two characteristic Raman shifts of graphitic structure. The intensity ratios of D band to G band (I_D/I_G) of $Ni_3V_2O_8$/NG and Fe_2VO_4/NG are $\sim$1.11 and $\sim$1.65, respectively, indicating the graphene oxide is reduced to graphene successfully during the hydrothermal process.
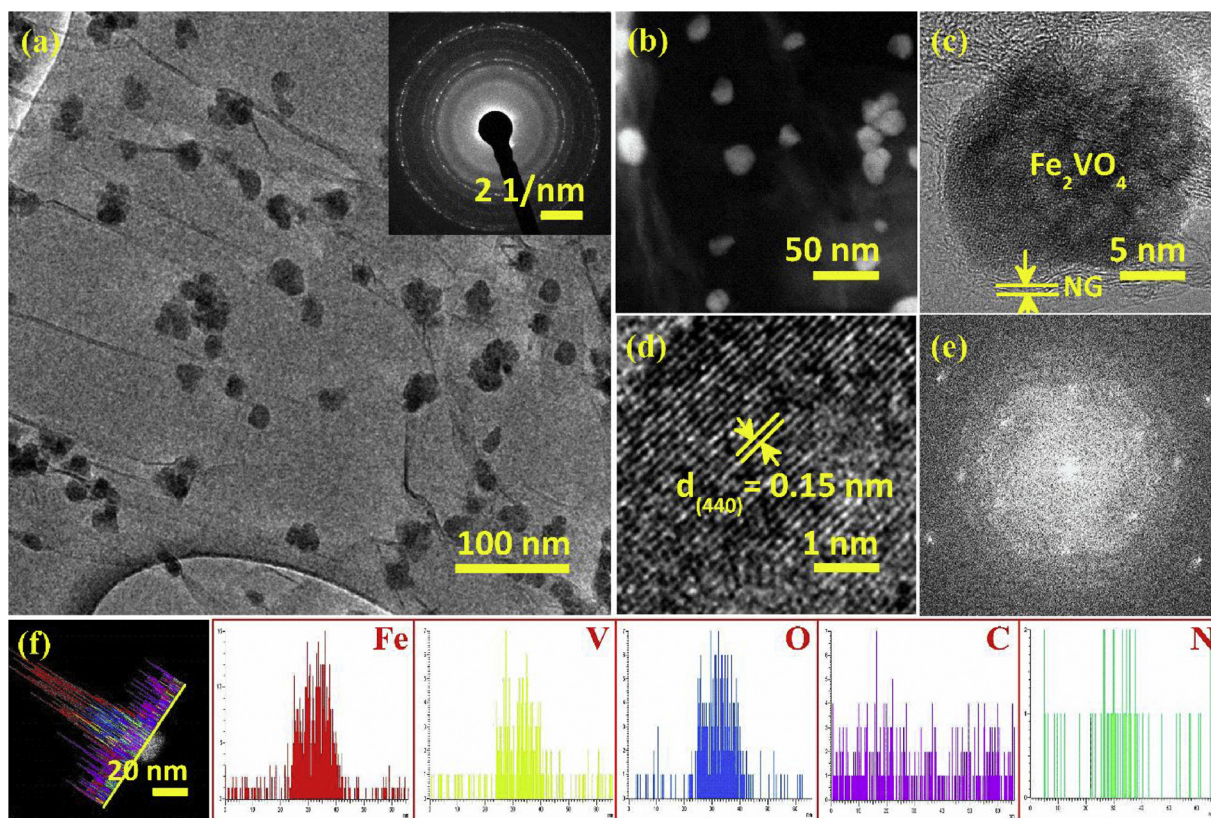
Fig. 3. (a) TEM image (inset shows the corresponding SAED pattern), (b) STEM image, (c, d) HR-TEM images, (e) FFT pattern, and (f) STEM-EDS line mapping images of Fe$_2$VO$_4$/NG hybrid.

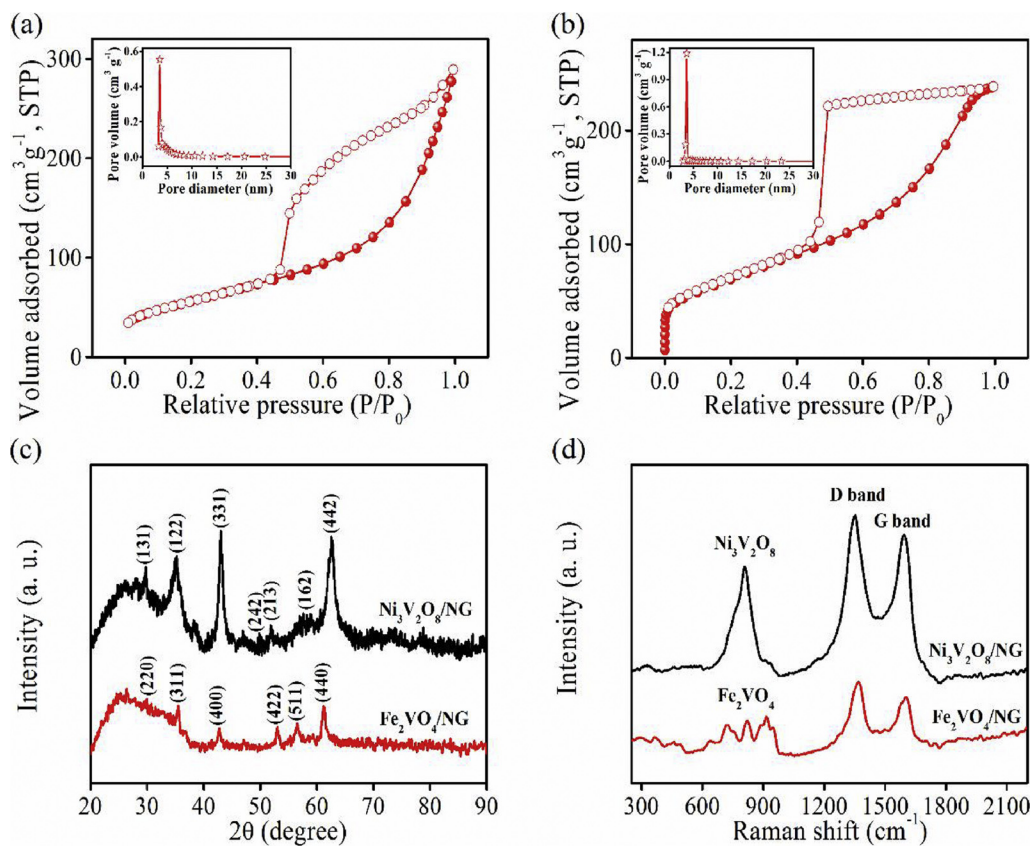**Fig. 4.** N$_2$ sorption isotherms of (a) Ni$_3$V$_2$O$_8$/NG and (b) Fe$_2$VO$_4$/NG hybrids (inset shows the corresponding BJH pore size distribution plot), (c) XRD pattern, and (d) Raman spectra of Ni$_3$V$_2$O$_8$/NG and Fe$_2$VO$_4$/NG hybrids.
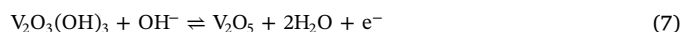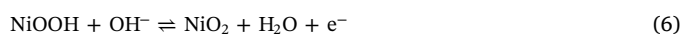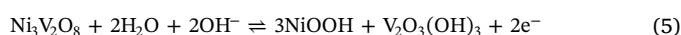
Furthermore, additional peak at around 800 cm^{-1} is observed, which is belong to the characteristic Raman shift of Ni$_3$V$_2$O$_8$ NPs [36]. In the case of Fe$_2$VO$_4$/NG hybrid, the Raman shifts in the range of 600–1000 cm^{-1} are attributed to the characteristic bands of Fe$_2$VO$_4$ NPs [37].

To obtain the optimized Ni$_3$V$_2$O$_8$/NG hybrid, the crystal structure of Ni$_3$V$_2$O$_8$/NG with various mass ratio of mixed metal precursors: GO (2.5:1 and 7.5:1) have also been synthesized and examined, as shown in Fig. S7. The Ni$_3$V$_2$O$_8$/NG hybrid in different mass ratios display the same crystal planes, confirming the successful synthesis of Ni$_3$V$_2$O$_8$/NG hybrid without any impurities was observed. N$_2$ sorption isotherms of Ni$_3$V$_2$O$_8$/NG (2.5:1 and 7.5:1) show the type-IV feature, which is well-consistent Ni$_3$V$_2$O$_8$/NG (5:1) (Fig. S8a and b). The BJH pore size distribution shows the pore size of ~3.9 nm and ~3.4 nm, respectively, representing the mesoporous configuration. Additionally, the BET specific surface area of Ni$_3$V$_2$O$_8$/NG (2.5:1) and Ni$_3$V$_2$O$_8$/NG (7.5:1) are of ~207 m^2 g^{-1} and ~198 m^2 g^{-1}, respectively. Remarkably, the specific surface area is reduced with the increase of metal mass loadings in the hybrid architecture. As we know that, the large specific surface area of electrode materials undoubtedly could shorten the ion/electron transfer pathways and increase the utilization of active sites, which endow the electrode materials with enhanced electrochemical performance. However, the specific capacitance of Ni$_3$V$_2$O$_8$/NG (5:1) is superior to that of Ni$_3$V$_2$O$_8$/NG (2.5:1) and Ni$_3$V$_2$O$_8$/NG (7.5:1) (Fig. S8c). To further understand this result with EIS study, Nyquist plots of Ni$_3$V$_2$O$_8$/NG electrode with different samples are shown in Fig. S8d. The Ni$_3$V$_2$O$_8$/NG (5:1) electrode shows the lowest charge transfer resistance (R$_{ct}$) comparing to the others (Ni$_3$V$_2$O$_8$/NG (2.5:1) and Ni$_3$V$_2$O$_8$/NG (7.5:1)), demonstrating the most predominant electrical conductivity of this electrode. The Ni$_3$V$_2$O$_8$/NG (7.5:1) shows a lower specific capacitance and a smaller specific surface area than Ni$_3$V$_2$O$_8$/NG (5:1) due to high loading of Ni$_3$V$_2$O$_8$ NPs reduce the conductivity as well as utilization of the active electrocatalyst during electrochemical performance. This result has also been demonstrated by the FE-SEM analysis, as shown in Fig. S3. The FE-SEM images of Ni$_3$V$_2$O$_8$/NG (7.5:1) displays that more agglomerated Ni$_3$V$_2$O$_8$ NPs over the NG support. However, the mass loading of the active materials is lower (Ni$_3$V$_2$O$_8$/NG (2.5:1)), resulting the poor capacitive performance. As a result, the mass ratios of metal precursors: GO is a key factor to attain the high performance of SCs in real time applications. Therefore, we conclude that the metal precursors: GO mass ratio 5: 1 of the hybrid material is optimum ratio for construct the ASC in practical applications.

To investigate the elemental composition and valences of Ni$_3$V$_2$O$_8$/NG and Fe$_2$VO$_4$/NG hybrids, XPS analysis were conducted, as shown in Fig. 5. The survey spectra of Ni$_3$V$_2$O$_8$/NG in Fig. 5a shows that the presence of Ni 2p, V 2p, O 1 s, C 1 s and N 1 s in the Ni$_3$V$_2$O$_8$/NG hybrid, demonstrating the successful synthesis of Ni$_3$V$_2$O$_8$/NG hybrid in the current synthesis technique. The amount of nitrogen in the Ni$_3$V$_2$O$_8$/NG hybrid is around ~7.9 at. %. The high-resolution N 1 s spectrum (Fig. S9a) deconvoluted into four peaks located at ~398.8 eV, ~399.3 eV, ~400.2 eV, ~402.2 eV, corresponding to the Pyridinic N, Pyrrolic N, Graphitic N and Pyridine N-oxide, respectively [38]. These results reveal that the effective doping of N atom into graphene framework. High-resolution Ni 2p spectrum (Fig. 5b) shows that the main peaks at ~856.3 eV and ~874 eV, which corresponds to the Ni 2p$_{3/2}$ and Ni 2p$_{1/2}$, respectively [37]. The Ni 2p$_{3/2}$ and Ni 2p$_{1/2}$ are divided to two separating peaks, confirming the presence of Ni^{2+} and Ni^{3+} states in the Ni$_3$V$_2$O$_8$/NG hybrid. The deconvoluted V 2p (Fig. 5c) shows two doublets for spin-orbits V 2p$_{3/2}$ and V 2p$_{1/2}$, which can be divided as V^{4+} and V^{5+} oxidation states, respectively [39]. These results demonstrate the multiple valences in the Ni$_3$V$_2$O$_8$/NG hybrid structure that facilitate the Faradaic reaction to enhance the electrochemical properties of the SCs. The survey XPS spectrum of Fe$_2$VO$_4$/NG (Fig. 5d) confirms the composition of Fe$_2$VO$_4$/NG. The amount of nitrogen in the Fe$_2$VO$_4$/NG hybrid is around ~6.2 at. %. The high-resolution N 1 s spectrum of Fe$_2$VO$_4$/NG hybrid shows the Pyridinic N, Pyrrolic N,

Graphitic N and Pyridine N-oxide with the binding energies of ~398.3 eV, ~399.5 eV, ~400 eV and ~402.6 eV, respectively (Fig. S10b). The high-resolution Fe 2p spectrum (Fig. 5e) displays the Fe 2p$_{3/2}$ centered at ~711.2 eV, and Fe 2p$_{1/2}$ centered at ~724.8 eV with the additional peaks of their shake-up satellite peaks at ~715.5 eV, ~719.3 eV and ~733.2 eV [40]. The divided peaks of both Fe 2p$_{3/2}$ and Fe 2p$_{1/2}$ indicate the oxidation states of Fe^{2+} and Fe^{3+}. The V 2p spectrum of Fe$_2$VO$_4$/NG hybrid with V 2p$_{3/2}$ and V 2p$_{1/2}$ also reveals the multiple valences of V^{4+} and V^{5+} (Fig. 5f).

To investigate the feasibility of Ni$_3$V$_2$O$_8$/NG cathode and Fe$_2$VO$_4$/NG anode for solid-state ASCs, the electrochemical investigations of each electrode was examined using the three-electrode configuration in aqueous 3 M KOH electrolyte. Fig. 6a depicts the typical CV curves of Ni$_3$V$_2$O$_8$/NG electrode with potential window from −0.1 to 0.6 V at different sweep rates from 10–100 mV s^{-1}. All the CV curves show the strong redox peaks, indicating that the capacitive performance is governed by faradic reactions. The possible electrochemical energy storage mechanism is proposed as follows:

$$Ni_3V_2O_8 + 2H_2O + 2OH^- \rightleftharpoons 3NiOOH + V_2O_3(OH)_3 + 2e^- \tag{5}$$

$$NiOOH + OH^- \rightleftharpoons NiO_2 + H_2O + e^- \tag{6}$$

$$V_2O_3(OH)_3 + OH^- \rightleftharpoons V_2O_5 + 2H_2O + e^- \tag{7}$$

Even at the high scan rate of 100 mV s^{-1}, the CV curves keep a regular redox peak, suggesting that the outstanding rate capability of Ni$_3$V$_2$O$_8$/NG electrode. For comparison, NiO/NG and V$_2$O$_5$/NG hybrids were synthesized, and detail investigation was carried out and illustrated in Figs. S11 and S12. The CV curves of NiO/NG, V$_2$O$_5$/NG, and Ni$_3$V$_2$O$_8$/NG electrodes at a constant scan rate of 30 mV s^{-1} are shown in Fig. S13. Remarkably, the CV area of Ni$_3$V$_2$O$_8$/NG electrode is larger than that of NiO/NG and V$_2$O$_5$/NG electrodes, indicating the Ni$_3$V$_2$O$_8$/NG holds an excellent electrochemical performance. Such electrochemical properties are due to the synergic contribution from both nickel and vanadium with mixed valences, which can promote more redox reaction and predominant electric conductivities. The GCD tests were performed at different current densities from 1 to 30 A g^{-1} (Fig. 6b), in which the voltage plateaus appeared between 0.2 and 0.3 V, further confirming the Faradaic characteristic of Ni$_3$V$_2$O$_8$/NG electrode [9]. According to the GCD curves, the specific capacitances of Ni$_3$V$_2$O$_8$/NG were calculated and are shown in Fig. 6c. The Ni$_3$V$_2$O$_8$/NG electrode exhibited high specific capacitances of ~1898, 1827, 1731, 1578, 1481, 1346 and 1238 F g^{-1} at the current densities of 1, 3, 5, 8, 10, 20 and 30 A g^{-1}, respectively. Even though, the specific capacitance gradually decreased with increase of current densities due to the rising voltage drop, the Ni$_3$V$_2$O$_8$/NG electrode still delivered an extraordinary capacitive performance ~1238 F g^{-1} at a high current density of 30 A g^{-1}. This high capacitance retention of ~65.2%, suggesting the predominant rate capability of Ni$_3$V$_2$O$_8$/NG electrode [41]. For comparison, NiO/NG and V$_2$O$_5$/NG electrodes examined by CV and GCD tests (Fig. S14). Both NiO/NG and V$_2$O$_5$/NG electrodes display the Faradic characteristics (Fig. S14a and c). However, based on the GCD curves in Fig. S14b and d, the specific capacitances of NiO/NG and V$_2$O$_5$/NG electrodes are ~1100 F g^{-1} and ~739 F g^{-1} at a current density of 1 A g^{-1}, respectively, which are obviously lower than that of Ni$_3$V$_2$O$_8$/NG electrode (Fig. S15a). EIS analysis was performed for the NiO/NG, V$_2$O$_5$/NG, and Ni$_3$V$_2$O$_8$/NG electrodes and are presented in Fig. S15b. All electrodes show arc line in the high-frequency region is related to the charge transfer resistance (R$_{ct}$) and a straight line in the low-frequency region related to the capacitive behavior of electrode materials in the Nyquist plots. Noticeably, the R$_{ct}$ of Ni$_3$V$_2$O$_8$/NG is ~0.6 Ω, which is much lower than NiO/NG (~1.7 Ω) and V$_2$O$_5$/NG (~2.2 Ω) electrodes, demonstrating the faster electron transport kinetics of Ni$_3$V$_2$O$_8$/NG due to the multiple redox reaction originated from the synergic interaction between nickel and vanadium ions in the Ni$_3$V$_2$O$_8$/NG hybrid. The straight line in the low-frequency region

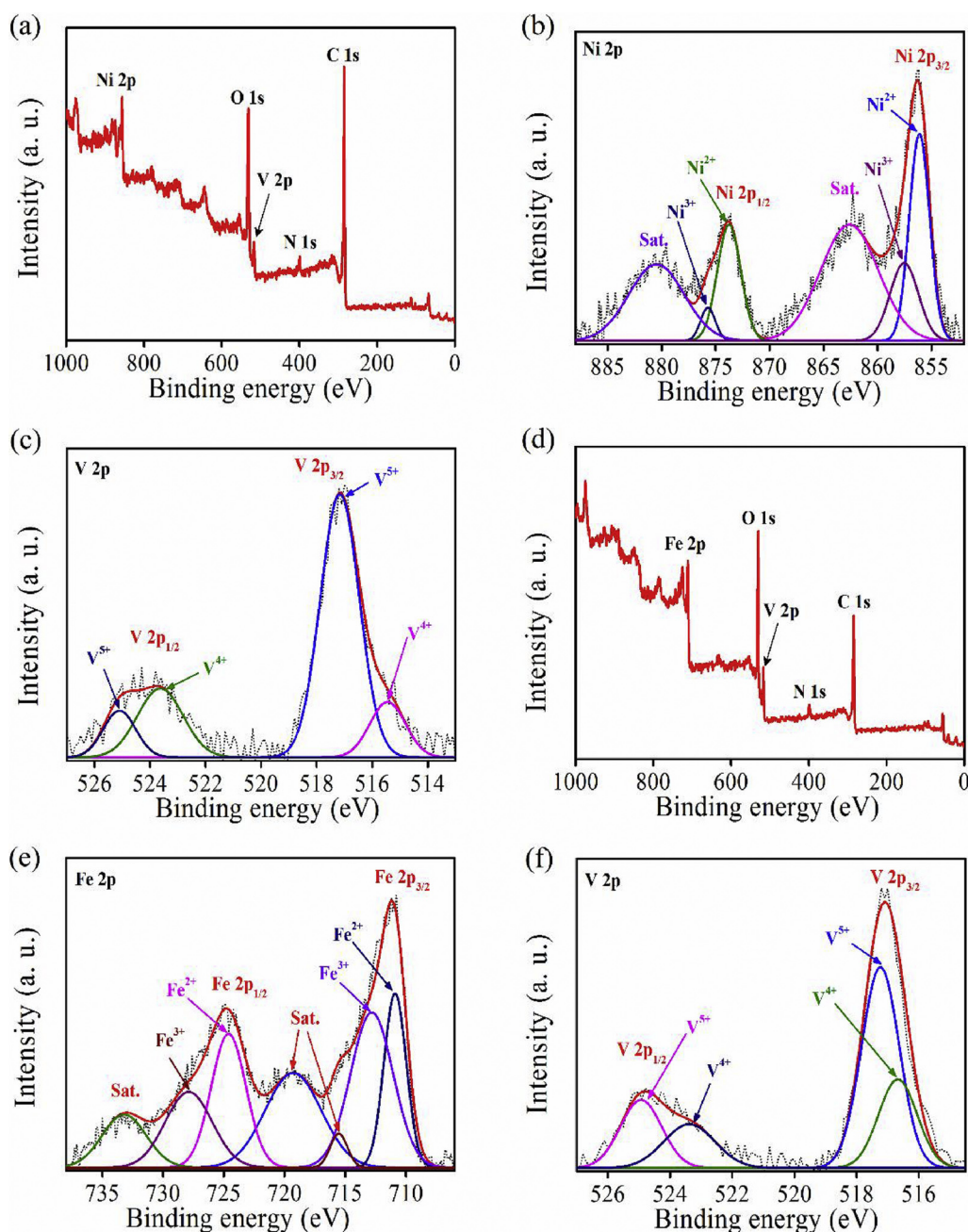**Fig. 5.** (a) XPS survey, (b) Ni 2p spectrum, (c) V 2p spectrum of $Ni_3V_2O_8$/NG hybrid, (d) XPS survey, (e) Fe 2p spectrum, and (f) V 2p spectrum of Fe_2VO_4/NG hybrid.

theoretically represents the capacitive behavior of electrode, representing the rapid ion transfer between electrode and electrolyte, also enhancing the capacitive performance of $Ni_3V_2O_8$/NG electrode. The internal resistance (R_s) decided by the intercept of the high-frequency region with the Z′-axis shows ~0.9 Ω, ~0.9 Ω and ~1.2 Ω, corresponding to the $Ni_3V_2O_8$/NG, NiO/NG and V_2O_5/NG electrodes, which is contributed from the ionic resistance of the electrolyte, intrinsic resistance of the substrate, and contact resistance at the interface of the active material/current collector. The $Ni_3V_2O_8$/NG electrode holds a lower value of both R_{ct} and R_s, demonstrating that the mixed oxidation states arising from individual nickel and vanadium ions in the $Ni_3V_2O_8$/NG facilitate the multiple redox reactions and accelerate the charge transfer rates, which effectively enhanced the Faradaic behavior of $Ni_3V_2O_8$/NG electrode [42,43].

Other than the excellent electrochemical properties, long-term cycle life is one of the critical issue in the practical utilization for ASCs. Fig.

S16 shows the cycling performance of $Ni_3V_2O_8$/NG electrode conducted in aqueous 3 M KOH electrolyte at the current density of 10 A g^{-1}. It's clearly observed that the capacitance retention of $Ni_3V_2O_8$/NG electrode retained ~87.1% after 10,000 consecutive charge-discharge cycles test. This result indicates the excellent cyclic stability of $Ni_3V_2O_8$/NG electrode superior to recently reported vanadium-based electrode materials in aqueous electrolyte [44,45]. This is due to the highly conductive NG network prevent the aggregation as well as reduce the degradation of active $Ni_3V_2O_8$ NPs from the electrolyte during the charge—discharge process that benefits to the substantial enhancement of electrochemical energy storage properties especially long-term cyclic life.

To construct the solid-state ASC device, the electrochemical performance of Fe_2VO_4/NG anode was also examined by electrochemical analysis. Fig. 6d shows the CV curves of Fe_2VO_4/NG electrode at different sweep rates from 10–50 mV s^{-1} with potential window from
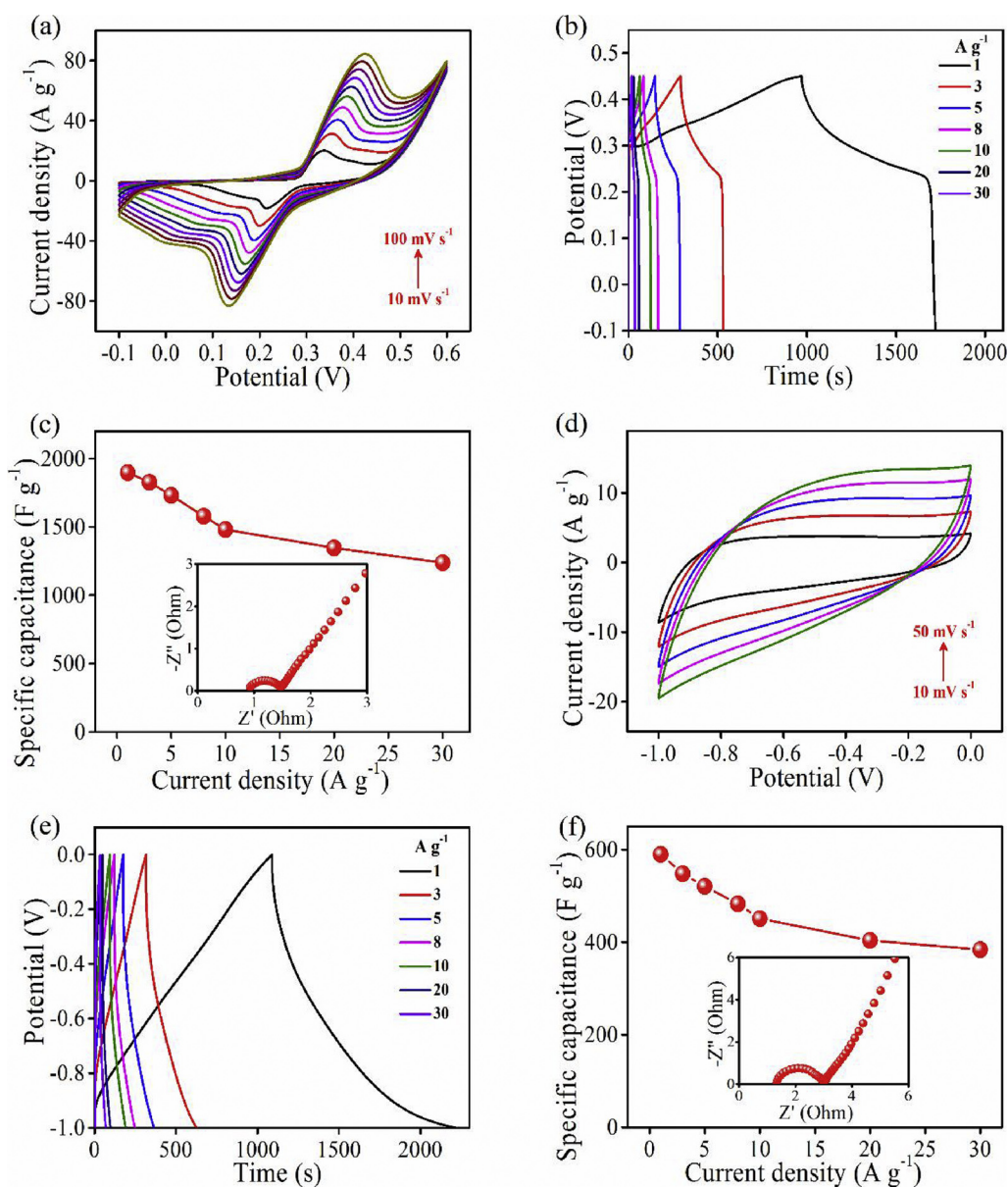
Fig. 6. (a) CV curves at different sweep rates (10–100 mV s^{-1}), (b) GCD curves at different current densities (1–30 A g^{-1}), (c) specific capacitance vs. current density of $Ni_3V_2O_8$/NG electrode (inset: Nyquist plots) of the $Ni_3V_2O_8$/NG electrode, (d) CV curves at different sweep rates (10–50 mV s^{-1}), (e) GCD curves at different current densities, and (f) specific capacitance vs. current density (inset: Nyquist plots) of the Fe_2VO_4/NG electrode.

−1.0 to 0 V. The Fe_2VO_4/NG electrode exhibits quasi-rectangular shape even at a high sweep rate, suggesting the ideal capacitive behavior at the applied potential window. The GCD curves of Fe_2VO_4/NG electrode were performed at different current densities from 1 to 30 A g^{-1} (Fig. 6e). The GCD curves show the regular triangular shape with almost linear–dependent voltage–time relationship, which is further confirmed the desirable capacitive property, which is well-consistent with CV curves. The negligible voltage drop was observed in the GCD curves implies the low internal resistance with improved electrochemical property of Fe_2VO_4/NG electrode. Fig. 6f displays the specific capacitance at different current densities that is calculated based on GCD curves. The Fe_2VO_4/NG electrode shows the high specific capacitances of ∼590, 548, 521, 483, 451, 404 and 384 F g^{-1} at the current densities of 1, 3, 5, 8, 10, 20 and 30 A g^{-1}, this distinct performance is comparable to the recently reported anode materials (Table S2). Apparently, the capacitance retention reaches to ∼65% even at a high current density of 30 A g^{-1} indicating that excellent rate capability of Fe_2VO_4/NG electrode. The EIS studies further interpreted the

predominant properties of Fe_2VO_4/NG electrode, as shown in inset of Fig. 6f. The R$_{ct}$ of Fe_2VO_4/NG electrode is ∼1.7 Ω obtained by the diameter of the semicircle in the high-frequency region, representing the ultra-fast electron transfer kinetics in the interface of active Fe_2VO_4 species and NG sheets [46]. The almost vertical line in the low-frequency region further confirms the ideal capacitive characteristics. Fig. S17 illustrates the cycling performance of Fe_2VO_4/NG electrode at the current density of 10 A g^{-1}. After 10,000 consecutive cycles in aqueous 3 M KOH electrolyte, ∼84.9% of its initial specific capacitance was retained, which reveals the outstanding cycling stability of Fe_2VO_4/NG.

To investigate the practical application in energy storage of SCs, the solid-state ASC device was constructed using $Ni_3V_2O_8$/NG as cathode and Fe_2VO_4/NG as anode materials in KOH/PVA gel electrolyte. Fig. 7a displays the CV curves of $Ni_3V_2O_8$/NG and Fe_2VO_4/NG electrodes performed at a constant scan rate of 50 mV s^{-1}. The $Ni_3V_2O_8$/NG electrode shows a remarkable faradic performance in the potential window of −0.1 to 0.6 V. While, Fe_2VO_4/NG displays a great capacitive performance in the potential window of −1.0 to 0 V. The cell voltage of

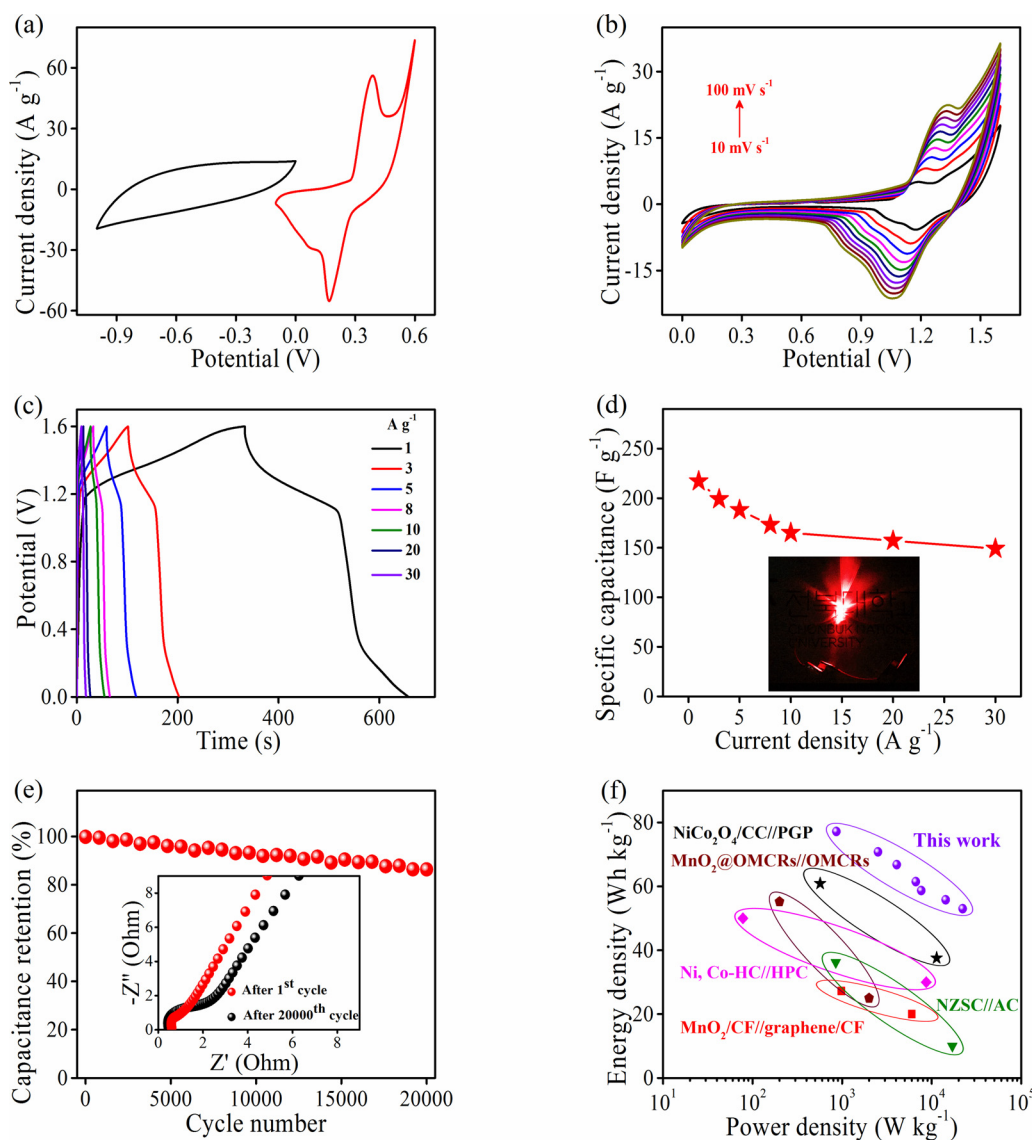**Fig. 7.** (a) CV curves of $Ni_3V_2O_8/NG$ and Fe_2VO_4/NG electrodes in a three-electrode configuration at $50\,mV\,s^{-1}$, (b) CV curves at different sweep rates ($10–100\,mV\,s^{-1}$), (c) GCD curves at different current densities ($1–30\,A\,g^{-1}$), (d) specific capacitance vs. current density (inset shows the glowing red LED), (e) cycling performance of $Ni_3V_2O_8/NG//Fe_2VO_4/NG$ ASC device at $10\,A\,g^{-1}$ for 20,000 cycles (inset: Nyquist plots after 1st and 20,000th cycles), and (f) Ragone plots of the $Ni_3V_2O_8/NG//Fe_2VO_4/NG$ ASC device. Data of recently reported ASC devices are shown for comparison (For interpretation of the references to colour in this figure legend, the reader is referred to the web version of this article).

the fabricated ASC device is expected to be extended to ~1.6 V taking advantages of the opposite potential range of $Ni_3V_2O_8/NG$ cathode and Fe_2VO_4/NG anode. The voltage window of ASC device was examined by testing the CV curves at a constant scan rate of $50\,mV\,s^{-1}$ and GCD analysis at a current density of $10\,A\,g^{-1}$ with various voltage ranges from 0–0.8 V to 0–1.6 V (Fig. S18). The voltage window can be extended up to 0–1.6 V as expected, and the ASC device is stable [47,48]. Therefore, the optimal cell voltage applied in ASC device is 0–1.6 V. The CV curves of ASC at the various sweep rates from $10–100\,mV\,s^{-1}$, as shown in Fig. 7b. All the CV curves show both capacitive and Faradaic behavior, indicating the excellent electrochemical performance was contributed from both $Ni_3V_2O_8/NG$ and Fe_2VO_4/NG electrodes. The CV curves keep a regular shape without obvious change as the increase of sweep rates, implying a fast charge–discharge process. The GCD curves at different current densities from 1 to $30\,A\,g^{-1}$ (Fig. 7c) depicts a nonlinear shape, suggesting that the Faradaic reactions play an important role in the capacitive properties. The corresponding specific capacitances at different current densities calculated according to the GCD curves are shown in Fig. 7d. The maximum specific capacitance of ASC reaches to ~217 F g^{-1} at the current density of $1\,A\,g^{-1}$, which is superior to that of recently reported ASCs [49,50]. The specific capacitance remains ~149 F g^{-1} at the high current density of $30\,A$ g^{-1} with capacitance retention of ~69%, revealing the outstanding

rate capability of the ASC. The practical feasibility of $Ni_3V_2O_8/NG//Fe_2VO_4/NG$ ASC device is verified by lightening a red LED (inset of Fig. 7d). Such great performance of ASC is contributed from both predominant property of $Ni_3V_2O_8/NG$ cathode and Fe_2VO_4/NG anode. Except for the great specific capacitance, the long-term cycling stability of ASC was tested at the current density of $10\,A\,g^{-1}$ (Fig. 7e). The capacitance retention of ASC achieved ~83.3% after 20,000 cycles. The cycling performance of the ASC is superior to three-electrode configuration in aqueous KOH electrolyte, which indicates that the solid-state electrolyte is more suitable for vanadium-based ASC. The EIS analysis (inset of Fig. 7e) further confirmed the outstanding cycling stability of $Ni_3V_2O_8/NG//Fe_2VO_4/NG$ ASC device. The R_{ct} of device increased only around 0.3 Ω after the 20,000th cycles. Such a high electrochemical performance and superior cycling stability of $Ni_3V_2O_8/NG//Fe_2VO_4/NG$ ASC is promising in the practical energy storage and comparable with those other reported solid-state ASCs.

Fig. 7f illustrates the Ragone plot of the $Ni_3V_2O_8/NG//Fe_2VO_4/NG$ ASC based on the GCD analysis. Noticeably, out fabricated ASC achieved the energy density of ~77.2 W h kg^{-1} at the power density of 863 W kg^{-1}, which shows a superior energy density. Even at a high-power density of ~22.186 kW kg^{-1}, the energy density still retains at 53 W h kg^{-1}, confirming the high rate performance of $Ni_3V_2O_8/NG//Fe_2VO_4/NG$ ASC device. The energy density of $Ni_3V_2O_8/NG//Fe_2VO_4/$

NG ASC is superior to the other reported solid-state ASCs, such as NiCo$_2$O$_4$/CC//PGP (60.9 W h kg^{-1} at the power density of 568 W kg^{-1}) [51], MnO$_2$/CF//graphene/CF (27.2 W h kg^{-1} at the power density of 980 W kg^{-1}) [52], Ni, Co-HC//HPC (50 W h kg^{-1} at the power density of 78 W kg^{-1}) [53], NZSC//AC (36.17 W h kg^{-1} at the power density of 850 W kg^{-1}) [54], and MnO$_2$@OMCRs//OMCRs (55.2 W h kg^{-1} at the power density of 200 W kg^{-1}) [55]. The exceptional supercapacitive performance make the solid-state Ni$_3$V$_2$O$_8$/NG//Fe$_2$VO$_4$/NG ASC device promising for modern electronics such as electric vehicles and portable electronic device.

4. Conclusion

A high-energy solid-state ASC device utilizing the bimetallic Ni$_3$V$_2$O$_8$/NG hybrid as cathode and Fe$_2$VO$_4$/NG hybrid as anode were successfully constructed. Both Ni$_3$V$_2$O$_8$/NG and Fe$_2$VO$_4$/NG hybrids with hierarchical nanostructure were synthesized by a simple, scalable and cost-effective in-situ hydrothermal technique. The Ni$_3$V$_2$O$_8$/NG electrode exhibited an excellent specific capacitance of ~1898 F g^{-1} at current density of 1 A g^{-1}, which is superior to NiO/NG and V$_2$O$_5$/NG electrodes. While, the Fe$_2$VO$_4$/NG with a large specific surface area of ~252 m^2 g^{-1} hold the maximum specific capacitance of ~590 F g^{-1} at a current density of 1 A g^{-1}, which is tremendously comparable with other reported anodic materials in SC applications. Remarkably, the assembled Ni$_3$V$_2$O$_8$/NG//Fe$_2$VO$_4$/NG ASC device achieved a predominant energy density of ~77.2 W h kg^{-1} at a power density of 863 W kg^{-1} and outstanding rate performance (~53 W h kg^{-1} at a power density of 22.186 kW kg^{-1}). Furthermore, the ASC device delivered an excellent cycling performance with high capacitance retention of ~83.3% after 20,000 consecutive charge-discharge cycles. Therefore, such encouraging solid-state Ni$_3$V$_2$O$_8$/NG//Fe$_2$VO$_4$/NG ASC device provide a great promise for power source in the energy storage systems in modern electronics.

Acknowledgements

Appendix A. Supplementary data

Supplementary material related to this article can be found, in the online version, at doi:https://doi.org/10.1016/j.apcatb.2018.08.026.

References

[1] Z.H. Pan, Y.C. Qiu, J. Yang, F.M. Ye, Y.J. Xu, X.Y. Zhang, M.N. Liu, Y.G. Zhang, Nano Energy 26 (2016) 610–619.
[2] T. Audichon, B. Guenot, S. Baranton, M. Cretin, C. Lamy, C. Coutanceau, Appl. Catal. B: Environ. 200 (2017) 493–502.
[3] B. Qiu, Q. Li, B. Shen, M. Xing, J. Zhang, 183 (2016) 216–223.
[4] J. Balamurugan, C. Li, S.G. Peera, N.H. Kim, J.H. Lee, Nanoscale 9 (2017) 13747–13759.
[5] M. Yu, Y. Zeng, Y. Han, X. Cheng, W. Zhao, C. Liang, X. Tong, H. Tang, X. Lu, Adv. Funct. Mater. 25 (2015) 3534–3540.
[6] X. Yang, H. Niu, H. Jiang, Q. Wang, F. Qu, J. Mater. Chem. A 4 (2016) 11264.
[7] Y. Zeng, Y. Han, Y. Zhao, Y. Zeng, M. Yu, Y. Liu, H. Tang, Y. Tong, X. Lu, Adv. Energy Mater. 5 (2015) 1402176.
[8] J. Balamurugan, T.D. Thanh, N.H. Kim, J.H. Lee, J. Mater. Chem. A 4 (2016) 9555–9565.
[9] S. Wang, H. Chen, G. Gao, T. Butburee, M. Lyu, S. Thaweesak, J.H. Yu, A. Du, G. Liu, L. Wang, Nano Energy 27 (2016) 627–637.
[10] G. Cabello, R.A. Davoglio, Appl. Catal. B: Environ. 218 (2017) 192–198.
[11] L. Shen, L. Yu, X.Y. Yu, X. Zhang, X.W. Lou, Angew. Chem. Int. Ed. 54 (2015) 1868–1872.
[12] Y. Chen, B. Liu, Q. Liu, J. Wang, Z. Li, X. Jing, L. Liu, Nanoscale 7 (2015) 15159–15167.
[13] B. Liu, B. Liu, Q. Wang, X. Wang, Q. Xiang, D. Chen, G. Shen, ACS Appl. Mater. Interfaces 5 (2013) 10011–10017.
[14] X. Lu, M. Yu, T. Zhai, G. Wang, S. Xie, T. Liu, C. Liang, Y. Tong, Y. Li, Nano Lett. 13 (2013) 2628–2633.
[15] M. Kan, D. Xue, A. Jia, X. Qian, D. Yue, J. Jia, Y. Zhao, Appl. Catal. B: Environ. 225 (2018) 504–511.
[16] J. Zhu, L. Cao, Y. Wu, Y. Gong, Z. Liu, H.E. Hoster, Y. Zhang, S. Zhang, S. Yang, Q. Yan, P.M. Ajayan, R. Vajtai, Nano Lett. 13 (2013) 5408–5413.
[17] L. Liu, J. Lang, P. Zhang, B. Hu, X. Yan, ACS Appl. Mater. Interfaces 8 (2016) 9335–9344.
[18] S. Samanta, R. Srivastava, Appl. Catal. B: Environ. 218 (2017) 621–636.
[19] J. Chen, J. Xu, S. Zhou, N. Zhao, C.P. Wong, Nano Energy 21 (2016) 145–153.
[20] Y. Song, T.Y. Liu, B. Yao, T.Y. Kou, D.Y. Feng, X.X. Liu, Y. Li, Small 13 (2017) 1700067.
[21] J. Balamurugan, G. Karthikeyan, T.D. Thanh, N.H. Kim, J.H. Lee, J. Power Sources 308 (2016) 149–157.
[22] C. Zhu, P. Yang, D. Chao, X. Wang, X. Zhang, S. Chen, B.K. Tay, H. Huang, H. Zhang, W. Mai, H.J. Fan, Adv. Mater. 27 (2015) 4566–4571.
[23] J. Balamurugan, S.G. Peera, M. Guo, T.T. Nguyen, N.H. Kiim, J.H. Lee, J. Mater. Chem. A 5 (2017) 17896–17908.
[24] Y. Zhang, W. Cui, W. An, L. Liu, Y. Liang, Y. Zhu, Appl. Catal. B: Environ. 221 (2018) 36–46.
[25] Y. Xu, Y. Mo, J. Tian, P. Wang, H. Yu, J. Yu, Appl. Catal. B: Environ. 181 (2016) 810–817.
[26] X. Zhou, L.J. Wan, Y.G. Guo, Adv. Mater. 25 (2013) 2152–2157.
[27] M. Guo, J. Balamurugan, T.D. Thanh, N.H. Kim, J.H. Lee, J. Mater. Chem. A 4 (2016) 17560–17571.
[28] L.Q. Mai, A.M. Khan, X. Tian, K.M. Hercule, Y.L. Zhao, X. Lin, X. Xu, Nat. Commun. 4 (2013) 2923–2930.
[29] E. Lim, C. Jo, M.S. Kim, M.H. Kim, J. Chun, H. Kim, J. Park, K.C. Roh, K. Kang, S. Yoon, J. Lee, Adv. Funct. Mater. 26 (2016) 3711–3719.
[30] J. Balamurugan, T.D. Thanh, S.B. Heo, N.H. Kim, J.H. Lee, Carbon 94 (2015) 962–970.
[31] S. Lu, K. Eid, D. Ge, J. Guo, L. Wang, H. Wang, H. Gu, Nanoscale 9 (2017) 1033–1039.
[32] M. Guo, J. Balamurugan, X. Li, N.H. Kim, J.H. Lee, Small 13 (2017) 1701275.
[33] P.Y. Tang, L.J. Han, A. Genc, Y.M. He, X. Zhang, L. Zhang, J.R.G. Mascaros, J.R. Morante, J. Arbiol, Nano Energy 22 (2016) 189–201.
[34] H. Xia, C. Hong, B. Li, B. Zhao, Z. Lin, Adv. Funct. Mater. 25 (2015) 627–635.
[35] J. Balamurugan, T.D. Thanh, N.H. Kim, J.H. Lee, Adv. Mater. Interfaces 3 (2016) 1500348.
[36] L. Niu, Y. Wang, F. Ruan, C. Shen, S. Shan, M. Xu, Z. Sun, C. Li, X. Liu, Y. Gong, J. Mater. Chem. A 4 (2016) 5669–5677.
[37] H. Mandal, S. Shyamal, P. Hajra, A. Bera, D. Sariket, S. Kundu, C. Bhattacharya, RSC Adv. 6 (2016) 4992–4999.
[38] E. Bayram, G. Yilmaz, S. Mukerjee, Appl. Catal. B: Environ. 192 (2016) 26–34.
[39] R. Sahoo, A. Pal, T. Pal, J. Mater. Chem. A 4 (2016) 17440–17454.
[40] J. Wang, C. Liu, J. Li, R. Luo, X. Hu, X. Sun, J. Shen, W. Han, L. Wang, Appl. Catal. B: Environ. 207 (2017) 316–325.
[41] P. Wu, S. Cheng, M. Yao, L. Yang, Y. Zhu, P. Liu, O. Xing, J. Zhou, M. Wang, H. Luo, M. Liu, Adv. Funct. Mater. 27 (2017) 1702160.
[42] J. Hong, Y.W. Lee, D. Ahn, S. Pak, J. Lee, A.R. Jang, S. Lee, B. Hou, Y. Cho, S.M. Morris, H.S. Shin, S.N. Cha, J.I. Sohn, J.M. Kim, Nano Energy 39 (2017) 337–345.
[43] J. Yang, C. Yu, X. Fan, S. Liang, S. Li, H. Huang, Z. Ling, C. Hao, J. Qiu, Energy Environ. Sci. 9 (2016) 1299–1307.
[44] P.H. Jampani, O. Velikokhatnyi, K. Kadakia, D.H. Hong, S.S. Damle, J.A. Poston, A. Manivannan, P.N. Kumta, J. Mater. Chem. A 3 (2015) 8413–8432.
[45] F.K. Butt, M. Tahir, C. Cao, F. Idrees, R. Ahmed, W.S. Khan, Z. Ali, N. Mahmood, M. Tanveer, A. Mahmood, I. Aslam, ACS Appl. Mater. Interfaces 6 (2014) 13635–13641.
[46] G. Xiong, P. He, D. Wang, Q. Zhang, T. Chen, T.S. Fisher, Adv. Funct. Mater. 26 (2016) 5460–5470.
[47] J. Ji, L.L. Zhang, H. Ji, Y. Li, X. Zhao, X. Bai, X. Fan, F. Zhang, R.S. Ruo, ACS nano 7 (2013) 6237–6243.
[48] J. Balamurugan, C. Li, V. Aravindan, N.H. Kim, J.H. Lee, Adv. Funct. Mater. (2018) 1803287, , https://doi.org/10.1002/adfm.201803287.
[49] W. He, C. Wang, H. Li, X. Deng, X. Xu, T. Zhai, Adv. Energy Mater. (2017) 1700983.
[50] D.P. Dubal, N.R. Chodankar, R. Holze, D.H. Kim, P.G. Romero, ChemSusChem 10 (2017) 1771–1782.
[51] Z. Gao, W. Yang, J. Wang, N. Song, X. Li, Nano Energy 13 (2015) 306–317.
[52] N. Yu, H. Yin, W. Zhang, Y. Liu, Z. Tang, M.Q. Zhu, Adv. Energy Mater. 6 (2016) 1501458.
[53] Y. Zhao, H. Ma, S. Huang, X. Zhang, M. Xia, Y. Tang, Z.F. Ma, ACS Appl. Mater. Interfaces 8 (2016) 22997–23005.
[54] S. Wang, X. Wang, Z. Bao, X. Yang, L. Ye, L. Zhao, J. Mater. Chem. A 5 (2017) 10227–10235.
[55] P. Shang, J. Zhang, W. Tang, Q. Xu, S. Guo, Adv. Funct. Mater. 26 (2016) 7766–7774.